Silicon-aluminium phase transformation-induced superconducting rings

Brett C. Johnson,*,† Michael Stuiber,‡ Daniel L. Creedon,‡ Manjith Bose,‡ Amanuel Berhane,§ Laurens Henry Willems van Beveren,‡ Sergey Rubanov,‖ Jared H. Cole,† Vincent Mourik,§ Alexander R. Hamilton,§ Timothy L. Duty,§ and Jeffrey Colin McCallum‡

†*School of Science, RMIT University, VIC, 3001, Australia*

‡*School of Physics, University of Melbourne, VIC 3010, Australia*

¶*Melbourne Centre for Nanofabrication, VIC 3168, Australia*

§*School of Physics, University of New South Wales, Sydney, NSW, Australia*

‖*Ian Holmes Imaging Centre, Bio21 Institute, University of Melbourne, VIC, 3010, Australia*

E-mail: brett.johnson2@rmit.edu.au

Abstract

The development of devices that exhibits both superconducting and semiconducting properties is an important endeavour for emerging quantum technologies. We investigate superconducting nanowires fabricated on a silicon-on-insulator (SOI) platform. Aluminium from deposited contact electrodes is found to inter-diffuse with the Si nanowire along the entire length of the nanowire, over micron length scales and at temperatures well below the Al-Si eutectic. The phase transformed material is conformal with the predefined device patterns. The superconducting properties of a transformed mesoscopic ring formed on a SOI platform are investigated. Low temperature

magnetoresistance oscillations, quantized in units of the fluxoid, $h/2e$, are observed.

Keywords: Superconductivity, aluminium, nanowires, fluxoid quantization

The integration of superconductors within silicon devices is expected to greatly broaden opportunities in emerging quantum technologies.[1,2] Such hybrid devices are promising candidates to explore topological superconductivity and the possible existence of Majorana Fermions.[3,4] Further, unique architectures to couple spin qubits to superconducting microwave resonators[5,6] for qubit coupling for long range entanglement may also be possible.[7]

Approaches to obtain superconductivity in silicon-related materials and devices have generally relied on high concentration doping with boron, formation of alternative superconducting phases such as certain silicides, or proximity induced superconductivity.[8–10] Two general approaches to render Si superconducting are phase formation and a range of non-equilibrium techniques.[1] The non-equilibrium doping approach aims to incorporate an extremely high active boron concentration with gas-immersion laser doping[11] or ion implantation followed by annealing.[12–14] In contrast, the phase formation approach is commonly, although not exclusively, based on metal deposition followed by a thermal anneal to induce silicide or alloy formation. An advantage of this latter approach is the ease with which it can be implemented and that it is a common process in the formation of Ohmic contacts in microelectronics. Several superconducting silicon based compounds have been investigated using this process such as MoSi,[15] PtSi,[16] VSi[17] and Pt-Si/SiGe heterostructures.[18] More recently Al, which is a common choice for superconducting devices with its large coherence length, has been integrated with Ge-based semiconductors for quantum applications.[3,19–26] The fabrication of these hybrid devices often involves an elevated temperature step such as a photoresist bake or dielectric deposition which induces the inter-diffusion of the Al and Ge. This enables high contact transparency to be realised between the superconductor and the semiconductor materials.

Some of the main advantages of the phase transformation method are the ability to scale

the process, to have full control over the cross-sectional area of the device as well as its aspect ratio[15] and to form intimate contact between the superconducting and the semiconducting components of the device.

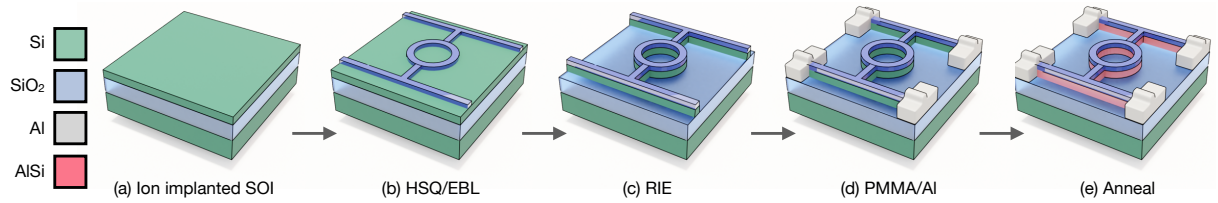

Figure 1: Schematic of the fabrication process used to form AlSi nanowires. (a) SOI with a highly doped 50 nm top layer is used. (b) Si nanowire patterning is achieved with EBL of HSQ followed by (c) RIE. (d) Al is deposited over the Si contact pad areas using a PMMA mask. (e) The final 450°C anneal induces Al migration throughout the device.

In this work, we describe a Si nanowire device fabrication process formed on a silicon-on-insulator (SOI) platform. Electrical contact pads are formed by aluminium (Al) deposition. During a low temperature anneal at 450°C the Al was found to migrate throughout the entire device, even over micron length scales, forming an Al device that conforms to the initial Si nanowire geometry. The transformed Al device may contain a small concentration of Si (<2 at.%). This results in a higher critical temperature (1.54 K) and critical magnetic field than that expected of a deposited Al nanowire with similar dimensions. This allows a larger range of parameter space to be studied. The Al transformed Si nanowire will thus be referred to as an AlSi nanowire herein. This behaviour was confirmed in five devices in two different batches. The main device discussed here consists of a superconducting AlSi ring with a wire cross-section of 50×50 nm^2 and an inner radius of 200 nm which produces periodic oscillations of the critical temperature T_c as the strength of a magnetic field threading the ring is varied. This is consistent with the Little-Parks effect, .[27–30] The device has an extremely high quality factor as evidenced through the high critical current I_C (2.8 A/cm^2), large super-current/re-trapping-current hysteresis and current-voltage (IV) characteristics.

Device fabrication

A schematic of the device fabrication process is shown in Fig. 1. We start with a SOI platform with 50 nm Si (100) on 150 nm SiO_2 (buried oxide, BOX) on bulk Si. Both the top Si layer and the substrate are Boron doped to a resistivity of $\rho = 1 - 20$ Ω.cm. The top Si layer was first degenerately doped using B ion implantation (6 keV, 1.7×10^{15} cm^{-2}). The ion energy was chosen so that the B was confined to the top Si layer. The B concentration is expected to peak at $4{\times}10^{20}$ cm^{-3}. The implanted dopants were electrically activated with a 600°C anneal for 10 minutes in a forming gas atmosphere (Ar with a 5% H content). Recrystallization occurred via solid phase epitaxy. This dopant concentration is not high enough to induce superconductivity.[11]

After the dopant activation anneal, 50 nm wide nanowire devices consisting of rings were patterned with electron beam lithography (EBL, Fig. 1(b)). Inner radii of 100, 200 or 400 nm were patterned. The 200 nm rings are the focus of this work but preliminary results from the other devices with 100 and 400 nm inner radii rings are provided in Fig. S2 of the Supporting Information. For the EBL, a 50 nm thick hydrogen silsesquioxane (HSQ) negative resist was used.

Reactive ion etching (RIE) was employed to transfer the pattern into the top Si layer to form the nanowire device (Fig. 1(c)). An additional EBL step using 600 nm Poly(methyl methacrylate) (PMMA) resist allowed patterning of the Al contact pads. Immediately before electron beam evaporation of a ∼175 nm thick Al layer (Fig. 1(d)), a buffered hydrofluoric acid dip was employed for 4 seconds to strip the HSQ and native oxide to ensure intimate contact between the Al and Si top layer. The HSQ over the other parts of the device was left in place. Alignment markers (5 nm titanium / 50 nm platinum) were used to align these two patterns. Finally, a thermal anneal at 450°C for 30 minutes under a forming gas atmosphere was performed as depicted in Fig. 1(e). This step induces Al migration throughout the entire device as discussed further below.

Structural characterization

A secondary electron microscopy (SEM) image of a fully fabricated 4-terminal device with

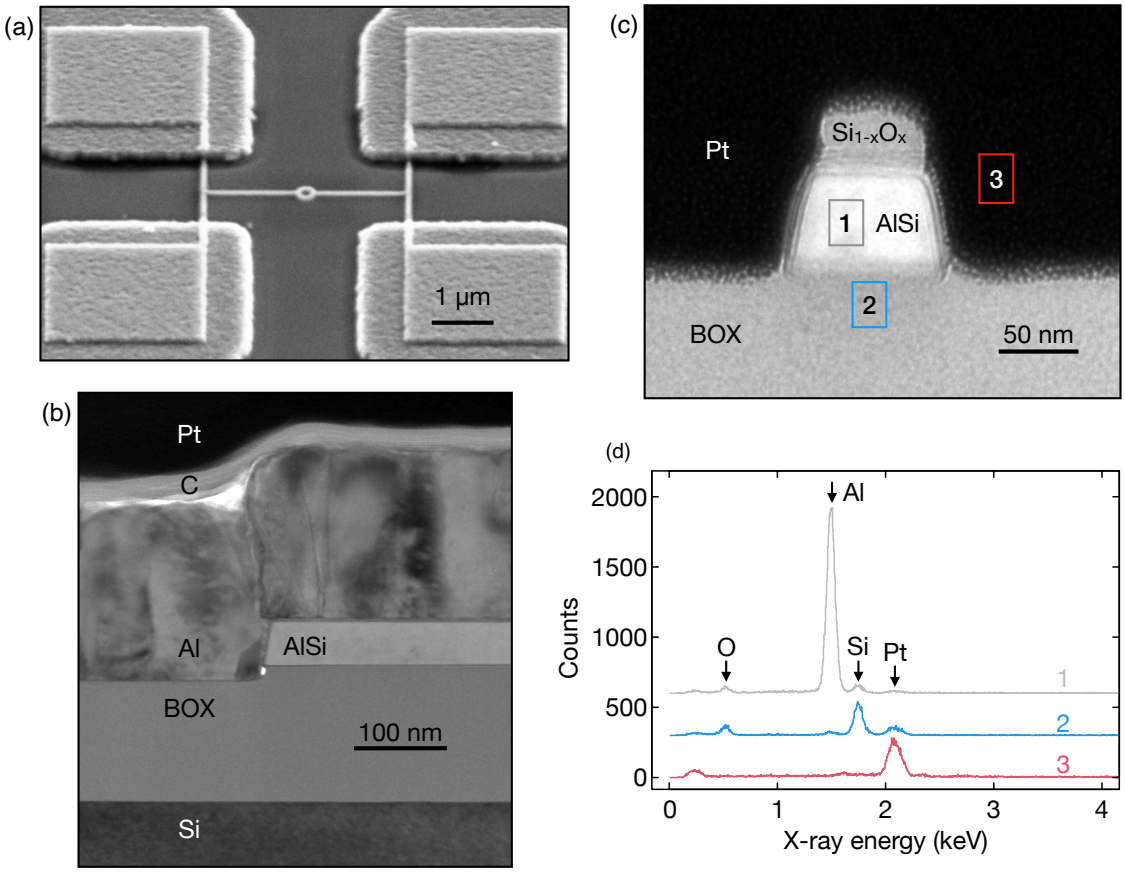

Figure 2: (a) SEM of the resultant device. The inner radius of the ring in this particular device is 100 nm. TEM cross-sections of (b) the contact pad and (c) the AlSi nanowire regions of the device. (d) Energy dispersive X-ray analysis measurements of the regions indicated in (c). The spectra have been offset vertically for clarity.

a ring of inner radius 100 nm is shown in Fig. 2(a). The cross-sectional TEM samples with a thickness of around 100 nm were prepared using a 30 keV FIB lift-off technique followed by a final etch with a 5 keV Ga FIB to reduce surface damage. Prior to the FIB milling, the areas of interest were protected with an electron-beam deposited 2 μm thick Pt film with some samples receiving a further carbon deposition beforehand. TEM images obtained with a FEI Tecnai TF20 TEM operated at 200 kV are presented in Fig. 2(b) and (c). These show cross sections through the contact pad and nano-wire portion of a device, respectively, after the 450°C anneal. Multiple boundaries can be discerned around the perimeter of the wire in 2(c) which is simply due to the TEM sampling a length of the nanowire. The HSQ layer from the lithography process (Fig. 1(b)) can also be clearly observed on top of the wire.

The stoichiometry of the nanowire after the anneal was investigated with energy dispersive X-ray spectroscopy (EDX) with a ∼1 nm diameter probe beam (EDAX Apollo XLT 2 detector (30 mm^2 active area, 0.3 sr collection angle). EDX spectra from selected areas indicated in Fig. 2(c) are presented in Fig. 2(d). Despite the small beam diameter, the spectra contain signals from outside the region probed due to elastic scattering of the electron beam. For instance, the 2.1 keV X-ray associated with Pt contributes to all spectra. However, the nanowire region is shown to consist mostly of Al which has been transported from the contact pads throughout the entire device during the 450°C anneal. This is well below the Si-Al binary eutectic temperature of 577°C.[31] It has recently been noted that the exchange rate between Al and Si can be enhanced as the width of the device is decreased which may explain the reaction we observe here.[32]

The transformed material also conforms to the geometry defined by the original Si nanowire and does not exhibit any significant volume change. This suggests that the Si does not remain in the nanowire but is transported towards the contact pads. The EDX spectrum contains a small Si signal equivalent to 2-6 at.% Si. A component of this is likely to contain contributions from the BOX and any thin SiO_2 shell that may exist at the periphery of the wire. The exact concentration of Si remaining in the wire is beyond our detection

capabilities at present but a small concentration after the Al-Si reaction may be expected.[33] Furthermore, in similar reactions involving Ge and Al in a nanowire geometry, detailed EDX analysis has revealed the formation of thin Ge diffusion channels near the wire surface.[34,35] These channels transport Ge towards the contact pad grain boundaries and surfaces. Similar behaviour has been noted for Ge/Si core shell nanowires and SiGe alloy nanowires.[36,37] A similar Si channel might then be expected in our devices.

The presence of Si in the transformed Al wire would have a profound impact on the superconducting properties of the device. As discussed in the next section, a superior superconducting critical field value is indeed measured in these devices compared to that expected of pure Al.[38] This indirectly supports the possibility of Si remaining in the nanowire.

Magnetoresistance characterization

Electrical measurements as a function of temperature and perpendicular magnetic field, $B_\perp$, were performed with a cryogen-free, closed-cycle dilution fridge equipped with a superconducting vector magnet. The stability of the sample temperature was assessed to have a variance of < 0.3 mK during measurement.

The four terminal 200 nm radius ring device was wire bonded in a non-standard way. One bond broke so the remaining bond on the same side of the ring was double bonded. This means that pure Al is also addressed in the device in addition to the AlSi nanowire and ring. Results from devices with a standard bonding configuration are included in Fig. S2 of the Supporting Information.

Figure 3 shows the 4-terminal lock-in resistance R for the 200 nm radius ring device measured with a phase-synchronized lock-in amplifier (SR830). The modulation current for the lock-in was 1 μA. The temperature dependence of R is shown for three different $B_\perp$ values in Fig. 3(a). At $B_\perp = 0$ T we observe two steps in resistance. The first at 1.54 K denotes the superconducting transition of the AlSi nanowire. The second step at 1.34 K is where the transition occurs for the Al pads. For the two higher $B_\perp$ values, only the AlSi-related transition is observed and the Al component of the device, in its normal state,

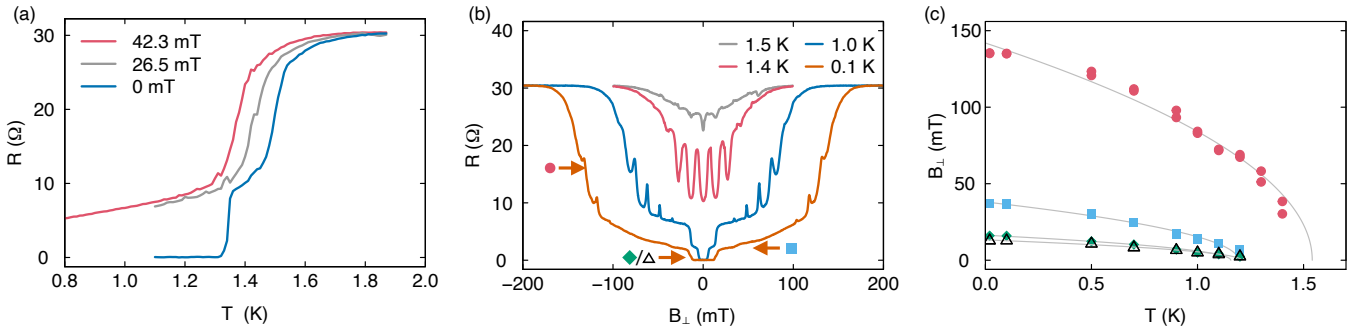

Figure 3: (a) The 200 nm AlSi ring 4-terminal resistance as a function of temperature with different applied $B_\perp$ fields. (b) $B_\perp$ dependence of the resistance at various temperatures. Two arrows indicate the point of inflection of the main resistive steps on the 0.1 K data set. (c) The critical field of the resistance steps extracted from (b). The solid lines are fits to the resistance steps at half height using Eq. 1.

provideing a series resistance contribution.

The $B_\perp$ dependence at temperatures between 0.1-1.5 K is shown in Fig. 3(b). Prominent resistance oscillations are observable which are strongest close to the normal-superconducting phase boundary and have a period of $B_\perp = (n + 1/2)\Phi_0$ where $\Phi_0 = 13.87$ mT.[39,40] From the relation $\Phi_\circ = h/2e = 13.87\pi r^2$, this period gives an effective ring radius of $r = 217.8$ nm which falls within the range of the nominal 200 nm and 250 nm inner and outer ring radii, respectively. For the other 100 and 400 nm inner radii rings we studied, we found values of 126 and 412 nm, respectively, again falling within the expected range (included in Fig. S2 of the Supporting Information). It can also be observed that the shape of the oscillations broaden with temperature. At higher temperatures their broad shape is similar to that observed for a SQUID.[41]

There are a number of resistance steps in the data presented in Fig. 3(b) indicated with arrows for the 0.1 K data set. The step at 14.5 mT is associated with the superconducting transition of the Al contact pad whereas the larger step around 135 mT corresponds to that of the AlSi component of the device. All resistance steps are well described by the equation:[42,43]

$$T_c(B_\perp) = T_c(0)\left(1 - \frac{\pi^2}{3}\left(\frac{w\xi B}{\Phi_0}\right)^2\right) \quad (1)$$

where the thickness is $w = 50$ nm for these nano-wires. The magnetic field position of a step is defined at its half height and the fits using this equation are included in Fig. 3(c) (solid lines). For the main resistance step that we associate with the AlSi rings, the coherence length and critical temperature at zero magnetic field are $\xi = 161 \pm 2$ nm and $T_c(0) = 1.54 \pm 0.03$ K, respectively. The BCS superconducting gap for AlSi is then 234 ± 5 μV using $\Delta = 1.764 k_B T_C$.[39] The inner step associated with the Al in the contact pads gives $T_c(0) = 1.21$ K and $\xi = 490 \pm 2$ nm assuming the layer thickness contributing to this feature is 175 nm thick (contact pad thickness).

Two other small resistance steps with fits shown in Fig. 3(c) could be discerned for this device between the Al and AlSi contributions with $\xi = 0.60$ and 1.39 μm and $T_c(0) = 1.19$ K and 1.16 K, respectively. These steps are likely associated with the AlSi leads of the device and an Al-rich component close to the Al contact pads, respectively. However, other possible sources of resistance such as charge noise in the underlying oxide or non-equilibrium quasi-particles cannot be ruled out at this stage.

Further insight can be gained via DC IV measurements. The IV traces were collected with a ramp generator to drive the current (SR DS345) between two contacts on opposite sides of the device, an amplifier to measure the bias voltage (SR560) between two additional contacts and an oscilloscope to digitize the output of the amplifier. A series of IV collected at 0.5 K is shown in Fig. 4(a) for $B_\perp$ values between 0 and 135 mT in steps of 5 mT. In these traces, only the increasing current ramps (supercurrent) are shown. The return currents, shown separately in Fig. 4(b), exhibit a re-trapping current at values much less than the critical current. This is due to self heating of the device at finite voltage values. The return current data will be presented in further detail below.

In Fig. 4(a), the critical current at zero field is 70 μA (2.8×10^{10} A/m^2). As the $B_\perp$ increases the Al pads go normal (from 10 mT) and contribute a resistive component ($\sim 2\ \Omega$)

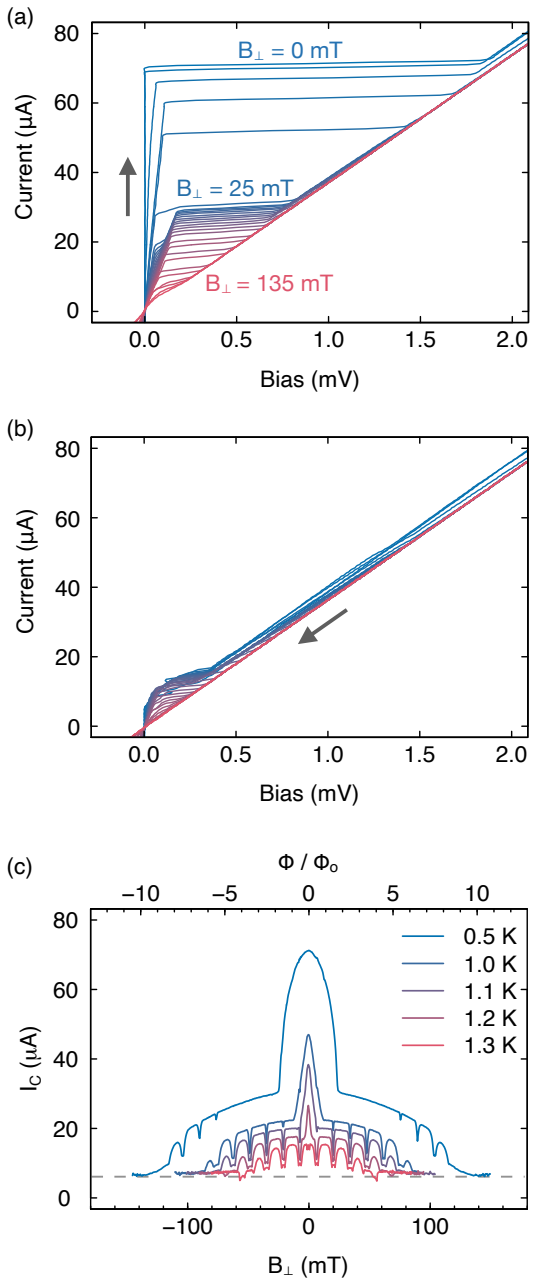

Figure 4: IV traces measured at 0.5 K for $B_\perp$ values between 0 and 135 mT in steps of 5 mT for (a) the super-current and (b) the re-trapping current. The current sweep direction is indicated with arrows. (c) Critical current as a function of $B_\perp$ extracted from IV data for temperatures between 0.5-1.3 K. No data is shown for $I < 7$ μA (dashed grey line) since reliable critical current values are more difficult to determine as explained in the text. The fluxoid values are indicated on the top axis.

to the device resulting in an increasing slope in the IV trace close to $V = 0$ V in Fig. 4(a). Another major resistive branch ($\sim 6\ \Omega$) appears above $B_\perp = 25$ mT corresponding to the

resistance steps indicated by the arrows in Fig. 3(b).

Figure 4(c) shows the critical current, I_C, as a function of $B_\perp$ for the 200 nm AlSi device at various temperatures. This was determined from the IV super-current traces like those displayed in Fig. 4(a). The trend as a function of $B_\perp$ displays clear oscillations with the same period as that observed with the lock-in method (Fig. 3). For $I < 7$ μA the dV and dI values are comparable to the noise so it becomes difficult to extract the switching current. As a consequence, the I_C values are not determined for $I_C < 7$ μA and the shape of some of the oscillations are not well defined, having a truncated dip.

To further investigate the resistive branches appearing in the IV traces we plot dV/dI in Fig. 5(a) and (b) for the super and return currents, respectively. In the normal phase $dV/dI = 27$ V/A for this device independent of field. Three dome-shaped components can be clearly discerned. The prominent central feature is associated with the superconducting phase of the Al contact pads. This feature denotes an operating region in which the device is fully superconducting, $dV/dI = 0$ V/A and is bound by large dV/dI values where the current switches to the normal phase. The prominence of this feature is expected to be a result of the electrical bonding configuration employed. Indeed, this feature is less pronounced in data from other devices where a standard four contact van der Pauw configuration was used (Fig. S2, Supporting Information). Furthermore, above 1.2 K, the critical temperature of Al, this feature disappears. The full data set consisting of dV/dI plots for both the super and return currents over a 0.5-1.5 K temperature range are provided in Fig. S3 of the Supporting Information for completeness.

Another broad dome-shaped feature extends to approximately $\pm$150 mT and is convoluted with oscillations at half integer values of Φ_0 from around 100 mT consistent with the resistance measurements of Fig. 3(b). This behaviour is also similar to a dc SQUID where the critical current is periodic with $B_\perp$ with the period inversely proportional to the area of the SQUID ring.[39] This feature is associated with the transformed AlSi.

The dV/dI plot in Fig. 5(a) also exhibits other more subtle features. For instance, there

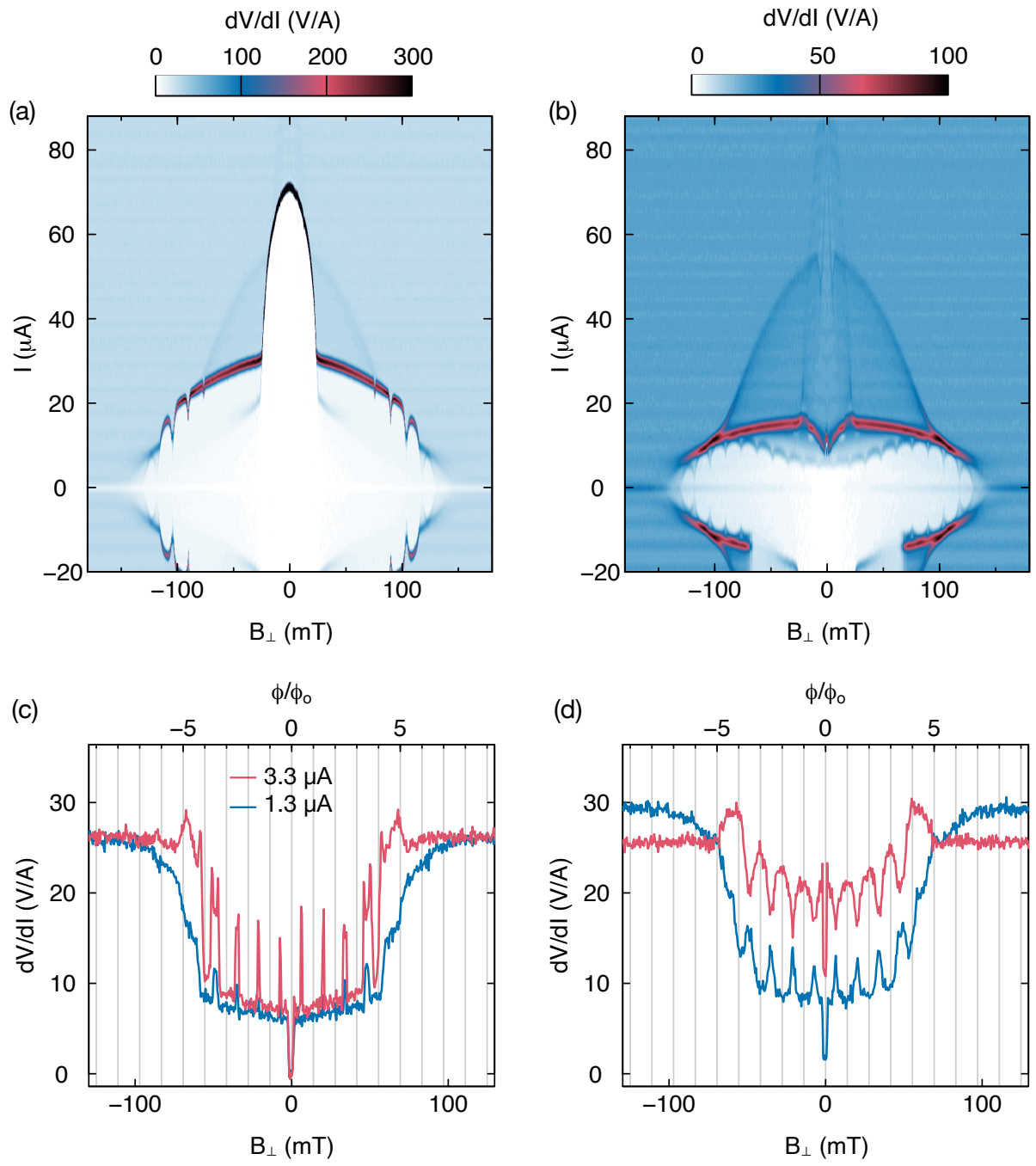

Figure 5: The 200 nm ring device dV/dI versus $B_\perp$ determined from the IV measured at 0.5 K for (a) the super-current and (b) the re-trapping current. dV/dI versus $B_\perp$ at 1.3 K for (c) the super-current and (d) the re-trapping current at 3.3 and 1.3 μA. The vertical lines denote the fluxoid values.

is a faint dome-shaped feature with a width of about ±80 mT. These may arise from the accidental formation of Josephson junctions or AlSi material with a variable stoichometry or cross-section which would have an impact on local superconducting properties such as the critical current.

The return current dV/dI also shows these features as displayed in Fig. 5(b). Interestingly, this includes the oscillations at half integer values of Φ_0. These are not as clearly defined as the super-current oscillations but appear over the full range of $B_\perp$ values within the AlSi superconducting phase. Furthermore, the return current oscillations are not superimposed over a domed shaped boundary as they are in Fig. 5(a). Instead, the envelope on which these oscillations appear first increases in critical current to a maxima at ±80 mT before decreasing again at higher fields. Such oscillations are not usually observed in the return current since it is a phenomenon characteristic of superconducting rings, not in the normal state.[40] However, there are some instances when return current oscillations are reported in the literature.[44] In our case, we see that the device transitions to a superconducting state before the oscillations arise as indicated by changes in dV/dI at current values greater than those where the oscillations appear in Fig. 5(b). This transition itself does not exhibit any oscillatory features. Therefore, although oscillations are observed in the return current, at least part of the device is already in a superconducting phase by this stage.

The shape of the oscillations is now considered. We plot dV/dI at a constant current in Figs. 5(c) and (d). These data were collected at the higher temperature of 1.3 K where the central Al feature is not as prominent (Al is in the normal state) and the oscillations are more clearly discerned across a broad range of $B_\perp$ values. Both the super- and the return currents dV/dI are displayed in Fig. 5(a) and (b), respectively. For the super-current dV/dI (Fig. 5(a)) very sharp peaks appear at $(n+1/2)\Phi_\circ$. The width of these peaks is around 1 mT but there is an apparent broadening as $B_\perp$ increases. Furthermore, the peak at ±48 mT is observed to split. This splitting is simply due to a resistive state transition of the device.

For the re-trapping dV/dI (Fig. 5(b)) the current can be chosen to either display standard

($I = 1.3$ μA) or inverted ($I = 3.3$ μA) oscillations, both with the $(n + 1/2)\Phi_\circ$ periodicity. We find that these more complex features are associated with the device being in a mixed superconducting and resistive states. This may have an impact on how the device might be used, for example, for magnetometry applications, but also may yield insight into complex oscillatory behaviour in mixed state devices.

In conclusion, a superconducting device was fabricated on a SOI platform using standard semiconductor industry processes. Al from the electrical contact pads was found to migrate throughout a pre-patterned Si nanowire device, even over micron length scales, forming an Al nanowire. The phase transformed material is conformal with the predefined device patterns and the resultant structures are exceptionally smooth-walled (as compared with the deposited Al contact pads). The impact of the top $Si_{1-x}O_x$ layer of the nanowire on device operation has not yet been fully explored. We speculate that Si rich channels close to the Si/SiO_2 interfaces may form to transport the Si out of the nanowire device. The exact structure has not yet been fully characterized but may be expected to have an impact on the superconducting properties of the device.

The temperature and magnetic field dependence of AlSi nano-ring devices displayed periodic features in the differential resistance as well as the critical current. These oscillations are a result of fluxoid quantization. The re-trapping current also exhibited oscillations.

Finally, with greater control over the Al migration process it may be possible to form junctions between AlSi and Si and to explore the possibility of Josephson tunnelling in a configuration that is different to the conventional thin insulating barrier Josephson junctions.

acknowledgement

This work is funded by an Australian Research Council (ARC) grant (DP200103233). We acknowledge the ARC Centre of Excellence for Quantum Computation and Communication Technology (CE170100012) for financial support. The AFAiiR node of the NCRIS Heavy Ion

Capability is also acknowledged for access to ion-implantation/ion-beam analysis facilities. M.S. acknowledges the Melbourne international fee remission scholarship (MISRF) and the Melbourne international research scholarship (MIRS). D.L.C. is supported by ARC grant DP190102852. J.H.C. is supported by the ARC Centre of Excellence FLEET (CE170100039) and the Australian National Computational Infrastructure facility. Finally, we thank Stephen Gregory for technical support.

References

(1) Shim, Y.-P.; Tahan, C. Bottom-up superconducting and Josephson junction devices inside a group-IV semiconductor. Nat. Commun. **2014**, 5, 4225.

(2) Blase, X.; Bustarret, E.; Chapelier, C.; Klein, T.; Marcenat, C. Superconducting group-IV semiconductors. Nat. Mater. **2009**, 8, 375–382.

(3) Ridderbos, J.; Brauns, M.; de Vries, F. K.; Shen, J.; Li, A.; Kölling, S.; Verheijen, M. A.; Brinkman, A.; van der Wiel, W. G.; Bakkers, E. P. A. M.; Zwanenburg, F. A. Hard Superconducting Gap and Diffusion-Induced Superconductors in Ge-Si Nanowires. Nano Lett. **2020**, 20, 122.

(4) Leijnse, M.; Flensberg, K. Introduction to topological superconductivity and Majorana fermions. Semicond. Sci. Technol. **2012**, 27, 124003.

(5) Kubo, Y.; Ong, F. R.; Bertet, P.; Vion, D.; Jacques, V.; Zheng, D.; Dréau, A.; Roch, J.-F.; Auffeves, A.; Jelezko, F.; Wrachtrup, J.; Barthe, M. F.; Bergonzo, P.; Esteve, D. Strong Coupling of a Spin Ensemble to a Superconducting Resonator. Phys. Rev. Lett. **2010**, 105, 140502.

(6) Amsüss, R.; Koller, C.; Nöbauer, T.; Putz, S.; Rotter, S.; Sandner, K.; Schneider, S.; Schramböck, M.; Steinhauser, G.; Ritsch, H.; Schmiedmayer, J.; Majer, J. Cavity QED with Magnetically Coupled Collective Spin States. Phys. Rev. Lett. **2011**, 107, 060502.

(7) Tosi, G.; Mohiyaddin, F. A.; Schmitt, V.; Tenberg, S.; Rahman, R.; Klimeck, G.; Morello, A. Silicon quantum processor with robust long-distance qubit couplings. Nat. Commun. **2017**, 8, 450.

(8) Bustarret, E. Superconductivity in doped semiconductors. Physica C **2015**, 514, 36–45.

(9) Blase, X.; Bustarret, E.; Chapelier, C.; Klein, T.; Marcenat, C. Superconducting group-IV semiconductors. Nature Materials **2009**, 8, 375–382.

(10) van Huffelen, W. M.; Klapwijk, T. M.; Heslinga, D. R.; de Boer, M. J.; van der Post, N. Carrier transport in mesoscopic silicon-coupled superconducting junctions. Phys. Rev. B **1993**, 47, 5170.

(11) Marcenat, C.; Kačmarčík, J.; Piquerel, R.; Achatz, P.; Prudon, G.; Dubois, C.; Gautier, B.; Dupuy, J. C.; Bustarret, E.; Ortega, L.; Klein, T.; Boulmer, J.; Kociniewski, T.; Débarre, D. Low-temperature transition to a superconducting phase in boron-doped silicon films grown on (001)-oriented silicon wafers. Phys. Rev. B **2010**, 81, 020501.

(12) Skrotzki, R.; Fiedler, J.; Herrmannsdörfer, T.; Heera, V.; Voelskow, M.; Mücklich, A.; Schmidt, B.; Skorupa, W.; Gobsch, G.; Helm, M.; Wosnitza, J. On-chip superconductivity via gallium overdoping of silicon. Appl. Phys. Lett. **2010**, 97, 192505.

(13) Skrotzki, R.; Herrmannsdörfer, T.; Heera, V.; Fiedler, J.; Mücklich, A.; Helm, M.; Wosnitza, J. The impact of heavy Ga doping on superconductivity in germanium. Low Temp. Phys **2011**, 37, 877–883.

(14) Herrmannsdörfer, T.; Heera, V.; Ignatchik, O.; Uhlarz, M.; Mücklich, A.; Posselt, M.; Reuther, H.; Schmidt, B.; Heinig, K.-H.; Skorupa, W.; Voelskow, M.; Wündisch, C.; Skrotzki, R.; Helm, M.; Wosnitza, J. Superconducting State in a Gallium-Doped Germanium Layer at Low Temperatures. Phys. Rev. Lett. **2009**, 102, 217003.

(15) Lehtinen, J. S.; Kemppinen, A.; Mykkänen, E.; Prunnila, M.; Manninen, A. J. Superconducting MoSi nanowires. Supercond. Sci. Technol. **2017**, 31, 015002.

(16) Oto, K.; Takaoka, S.; Murase, K.; Ishida, S. Superconductivity in PtSi ultrathin films. J. Appl. Phys. **1994**, 76, 5339–5342.

(17) Zhang, W.; Bollinger, A. T.; Li, R.; Kisslinger, K.; Tong, X.; Liu, M.; Black, C. T. Thin-film synthesis of superconductor-on-insulator A15 vanadium silicide. Sci. Rep. **2021**, 11, 2358.

(18) Tosato, A.; Levajac, V.; Wang, J.-Y.; Boor, C. J.; Borsoi, F.; Botifoll, M.; Borja, C. N.; Marti-Sanchez, S.; Arbiol, J.; Sammak, A.; Veldhorst, M.; Scappucci, G. Hard superconducting gap in a high-mobility semiconductor. 2022; `https://arxiv.org/abs/2206.00569`, arXiv.org e-Print archive. Accessed 2022-12-20.

(19) Xiang, J.; Vidan, A.; Tinkham, M.; Westervelt, R. M.; Lieber, C. M. Ge/Si nanowire mesoscopic Josephson junctions. Nat. Nanotechnol. **2006**, 1, 208–213.

(20) Su, Z.; Zarassi, A.; Nguyen, B. M.; Yoo, J.; Dayeh, S. A.; Frolov, S. M. High critical magnetic field superconducting contacts to Ge/Si core/shell nanowires. 2016; `https://arxiv.org/abs/1610.03010`, arXiv.org e-Print archive. Accessed 2022-12-20.

(21) Ridderbos, J.; Brauns, M.; Shen, J.; de Vries, F. K.; Li, A.; Bakkers, E. P. A. M.; Brinkman, A.; Zwanenburg, F. A. Josephson Effect in a Few-Hole Quantum Dot. Adv. Mater. **2018**, 30, 1802257.

(22) de Vries, F. K.; Shen, J.; Skolasinski, R. J.; Nowak, M. P.; Varjas, D.; Wang, L.; Wimmer, M.; Ridderbos, J.; Zwanenburg, F. A.; Li, A.; Koelling, S.; Verheijen, M. A.; Bakkers, E. P. A. M.; Kouwenhoven, L. P. Spin–Orbit Interaction and Induced Superconductivity in a One-Dimensional Hole Gas. Nano Letters **2018**, 18, 6483–6488.

(23) Hendrickx, N. W.; Franke, D. P.; Sammak, A.; Kouwenhoven, M.; Sabbagh, D.; Yeoh, L.; Li, R.; Tagliaferri, M. L. V.; Virgilio, M.; Capellini, G.; Scappucci, G.; Veldhorst, M. Gate-controlled quantum dots and superconductivity in planar germanium. Nature Communications **2018**, 9, 2835.

(24) Hendrickx, N. W.; Tagliaferri, M. L. V.; Kouwenhoven, M.; Li, R.; Franke, D. P.; Sammak, A.; Brinkman, A.; Scappucci, G.; Veldhorst, M. Ballistic supercurrent discretization and micrometer-long Josephson coupling in germanium. Phys. Rev. B **2019**, 99, 075435.

(25) Vigneau, F.; Mizokuchi, R.; Zanuz, D. C.; Huang, X.; Tan, S.; Maurand, R.; Frolov, S.; Sammak, A.; Scappucci, G.; Lefloch, F.; De Franceschi, S. Germanium Quantum-Well Josephson Field-Effect Transistors and Interferometers. Nano Letters **2019**, 19, 1023–1027.

(26) Hendrickx, N. W.; Lawrie, W. I. L.; Petit, L.; Sammak, A.; Scappucci, G.; Veldhorst, M. A single-hole spin qubit. Nature Communications **2020**, 11, 3478.

(27) Doll, R.; Näbauer, M. Experimental Proof of Magnetic Flux Quantization in a Superconducting Ring. Phys. Rev. Lett. **1961**, 7, 51–52.

(28) Deaver, B. S.; Fairbank, W. M. Experimental Evidence for Quantized Flux in Superconducting Cylinders. Phys. Rev. Lett. **1961**, 7, 43–46.

(29) Little, W. A.; Parks, R. D. Observation of Quantum Periodicity in the Transition Temperature of a Superconducting Cylinder. Phys. Rev. Lett. **1962**, 9, 9–12.

(30) Parks, R. D.; Little, W. A. Fluxoid Quantization in a Multiply-Connected Superconductor. Phys. Rev. **1964**, 133, A97–A103.

(31) Murray, J. L.; McAlister, A. J. The Al-Si (Aluminum-Silicon) system. Bull. Alloy Phase Diagr. **1984**, 5, 74.

(32) Wind, L.; Böckle, R.; Sistani, M.; Schweizer, P.; Maeder, X.; Michler, J.; Murphey, C. G. E.; Cahoon, J.; Weber, W. M. Monolithic and Single-Crystalline Aluminum–Silicon Heterostructures. ACS Appl. Mater. Interfaces **2022**, 14, 26238–26244.

(33) van Gurp, G. J. DiffusionâĂŘlimited Si precipitation in evaporated Al/Si films. J. Appl. Phys. **1973**, 44, 2040–2050.

(34) El hajraoui, K.; Luong, M. A.; Robin, E.; Brunbauer, F.; Zeiner, C.; Lugstein, A.; Gentile, P.; Rouvière, J.-L.; Den Hertog, M. In Situ Transmission Electron Microscopy Analysis of Aluminum–Germanium Nanowire Solid-State Reaction. Nano Letters **2019**, 19, 2897–2904.

(35) Brunbauer, F. M.; Bertagnolli, E.; Majer, J.; Lugstein, A. Electrical transport properties of single-crystal Al nanowires. Nanotechnology **2016**, 27, 385704.

(36) Sistani, M.; Luong, M. A.; den Hertog, M. I.; Robin, E.; Spies, M.; Fernandez, B.; Yao, J.; Bertagnolli, E.; Lugstein, A. Monolithic Axial and Radial Metal–Semiconductor Nanowire Heterostructures. Nano Lett. **2018**, 18, 7692–7697.

(37) Luong, M. A.; Robin, E.; Pauc, N.; Gentile, P.; Baron, T.; Salem, B.; Sistani, M.; Lugstein, A.; Spies, M.; Fernandez, B.; den Hertog, M. Reversible Al Propagation in SixGe1–x Nanowires: Implications for Electrical Contact Formation. ACS Appl. Nano Mater. **2020**, 3, 10427–10436.

(38) Chevrier, J.; Pavuna, D.; Cyrot-Lackmann, F. Electronic properties and superconductivity of rapidly quenched Al-Si alloys. Phys. Rev. B **1987**, 36, 9115–9121.

(39) Tinkham, M. Introduction to superconductivity; McGraw-Hill: New York, 1975.

(40) Bezryadin, A. Superconductivity in Nanowires: Fabrication and Quantum Transport; John Wiley & Sons, Ltd: Weinheim, Germany, 2012.

(41) Espy, C.; Sharon, O. J.; Braun, J.; Garreis, R.; Strigl, F.; Shaulov, A.; Leiderer, P.; Scheer, E.; Yeshurun, Y. Flux-periodicity crossover from h/2e to h/e in aluminium nano-loops. J. Phys. Conf. Ser. **2018**, 969, 012063.

(42) Tinkham, M. Effect of Fluxoid Quantization on Transitions of Superconducting Films. Phys. Rev. **1963**, 129, 2413–2422.

(43) Moshchalkov, V. V.; Gielen, L.; Strunk, C.; Jonckheere, R.; Qiu, X.; Haesendonck, C. V.; Bruynseraede, Y. Effect of sample topology on the critical fields of mesoscopic superconductors. Nature **1995**, 373, 319–322.

(44) Bruynseraede, Y.; Baert, M.; Bruyndoncx, V.; Chien, C. J.; Eom, J.; Metlushko, V. V.; Neuttiens, G.; Puig, T.; Rosseel, E.; Strunk, C.; Temst, K.; van Bael, M. J.; Chandrasekhar, V.; van Haesendonck, C.; Moshchalkov, V. V. New phenomena in nanostructured materials. Phys. Scr. **1996**, T66, 16–23.

TOC Graphic

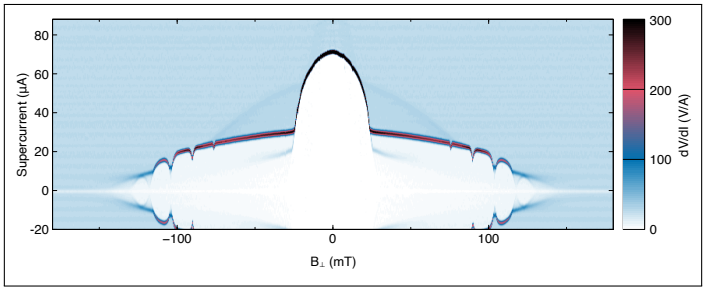
80
60
40
20
0
-20
Supercurrent (μA)
−100
0
100
B⊥ (mT)
300
200
100
0
dV/dI (V/A)

Supporting Information:

Silicon-aluminium phase transformation-induced superconducting rings

Brett C. Johnson,[1, a)] Michael Stuiber,[2, 3] Daniel L. Creedon,[2] Manjith Bose,[2] Amanuel Berhane,[4] Laurens Henry Willems van Beveren,[2] Sergey Rubanov,[5] Jared H. Cole,[1] Vincent Mourik,[4] Alexander R. Hamilton,[4] Timothy L. Duty,[4] and Jeffrey Colin McCallum[2]

[1)] *School of Science, RMIT University, VIC, 3001, Australia*

[2)] *School of Physics, University of Melbourne, VIC 3010, Australia*

[3)] *Melbourne Centre for Nanofabrication, VIC 3168, Australia*

[4)] *School of Physics, University of New South Wales, Sydney, NSW, Australia*

[5)] *Ian Holmes Imaging Centre, Bio21 Institute, University of Melbourne, VIC, 3010, Australia*

[a)] Electronic mail: brett.johnson2@rmit.edu.au

S1. STRUCTURAL CHARACTERISATION

Figure S1(a) shows a cross-sectional transmission electron microscopy (TEM) image of an AlSi nanowire fabricated by inducing Al migration through a silicon nanowire formed on a silicon on insulator platform. Energy dispersive X-ray analysis (EDX) is used to identify the composition of each component of the device. Fig. S1(b) shows that oxygen is present in the top HSQ layer of the wire. Fig. S1(c) shows the silicon and aluminium components. We suspect that the AlSi formation nucleates at the Si/SiO_2 interface, at the BOX and at the HSQ boundary, and proceeds epitaxially.

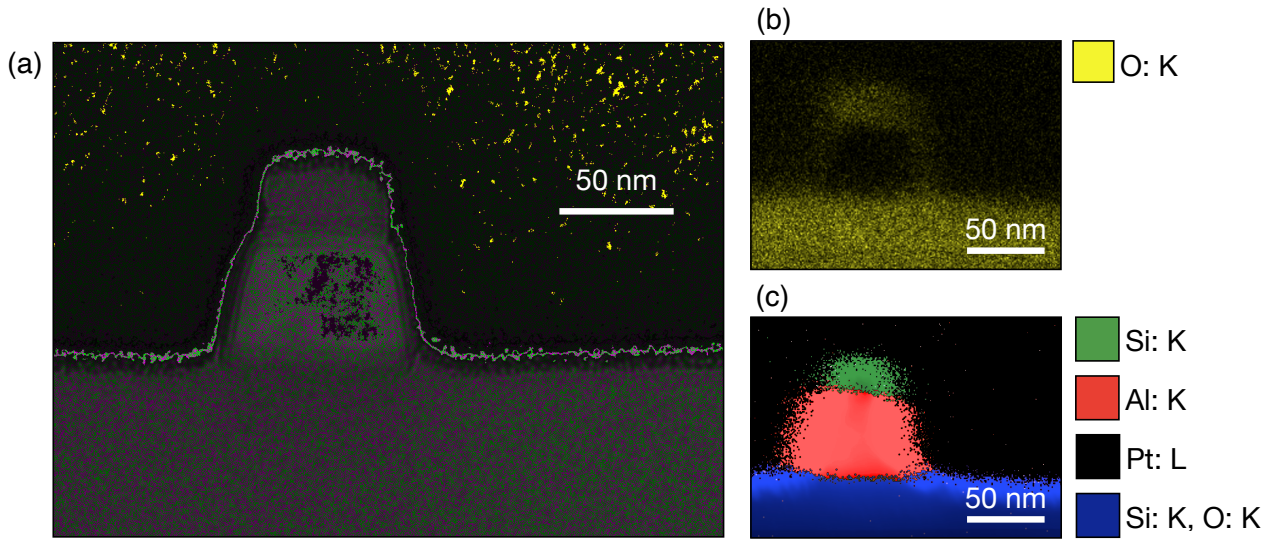

FIG. S1. (a) Cross-sectional transmission electron microscopy (TEM) image through a single AlSi nanowire. (b) The corresponding energy dispersive X-ray analysis image of the oxygen and (c) the silicon, aluminium and oxygen components within the nanowire. The green Si layer indicates the HSQ.

S2. MAGNETORESISTANCE MEASUREMENTS

Figure S2 shows the critical current as a function of applied magnetic field for devices with 100, 200 or 400 nm inner radii rings. The 100 and 400 nm devices were wire bonded in a standard van der Pauw configuration. One of the bonds on the 200 nm device broke during initial measurements. To progress with the measurement we double bonded one of

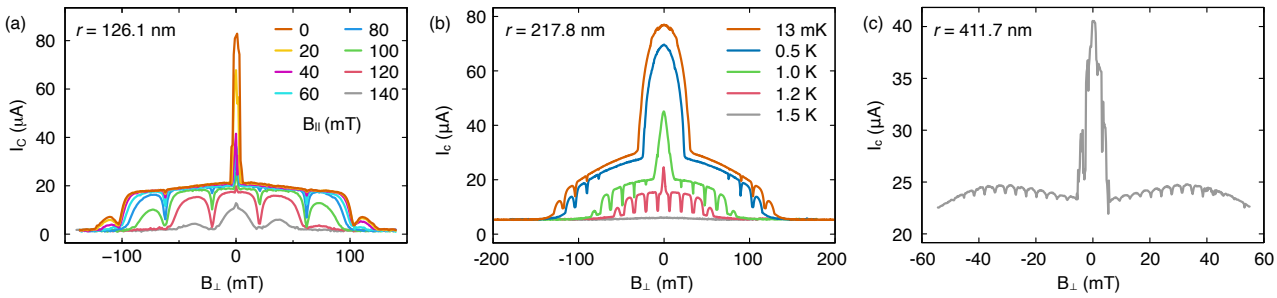

FIG. S2. Critical current for AlSi ring devices with nominal inner ring radii of (a) 100, (b) 200 and (c) 400 nm.

the contacts. As a consequence, the central feature which is due to thick Al in the contact pads is much more prominent in this device than the 100 and 400 nm devices.

Each device exhibits critical current dips at $B_\perp = (n + 1/2)\Phi_0$ as the perpendicular magnetic field, $B_\perp$ is varied with $\Phi_0 = 41.41$, 13.87, and 3.88 mT for the 100, 200 and 400 nm rings, respectively. From the relation $h/2e = \Phi_0 \pi r^2$,[1,2] these periods give an effective ring radii of $r = 126.1$, 217.8 and 411.7 nm which falls within the range of the nominal inner and outer ring radii. Data for the 100 nm ring in Fig. S2(a) includes measurements with the addition of a parallel field, $B_{||}$ in the range 0-140 mT. As $B_{||}$ increases the critical current dips become more pronounced.

S3. TEMPERATURE DEPENDENCE

The dV/dI plots extracted from the current-voltage traces for the super and return currents of the 200 nm device are displayed in Figs. S3 (a) and (b), respectively. The data were collected over a range of $B_\perp$ and temperatures. The critical current of the central dome-shaped feature between ± 10 mT decreases significantly as the temperature increases. It completely disappears between 1.2 and 1.3 K consistent with the T_c of pure Al. Likewise, the faint dome-shaped features which are clearly observed in Fig. S3(b) also disappear by a similar temperature.

Clear oscillations with $B_\perp$ can be discerned for both the super and return currents at each temperature studied.

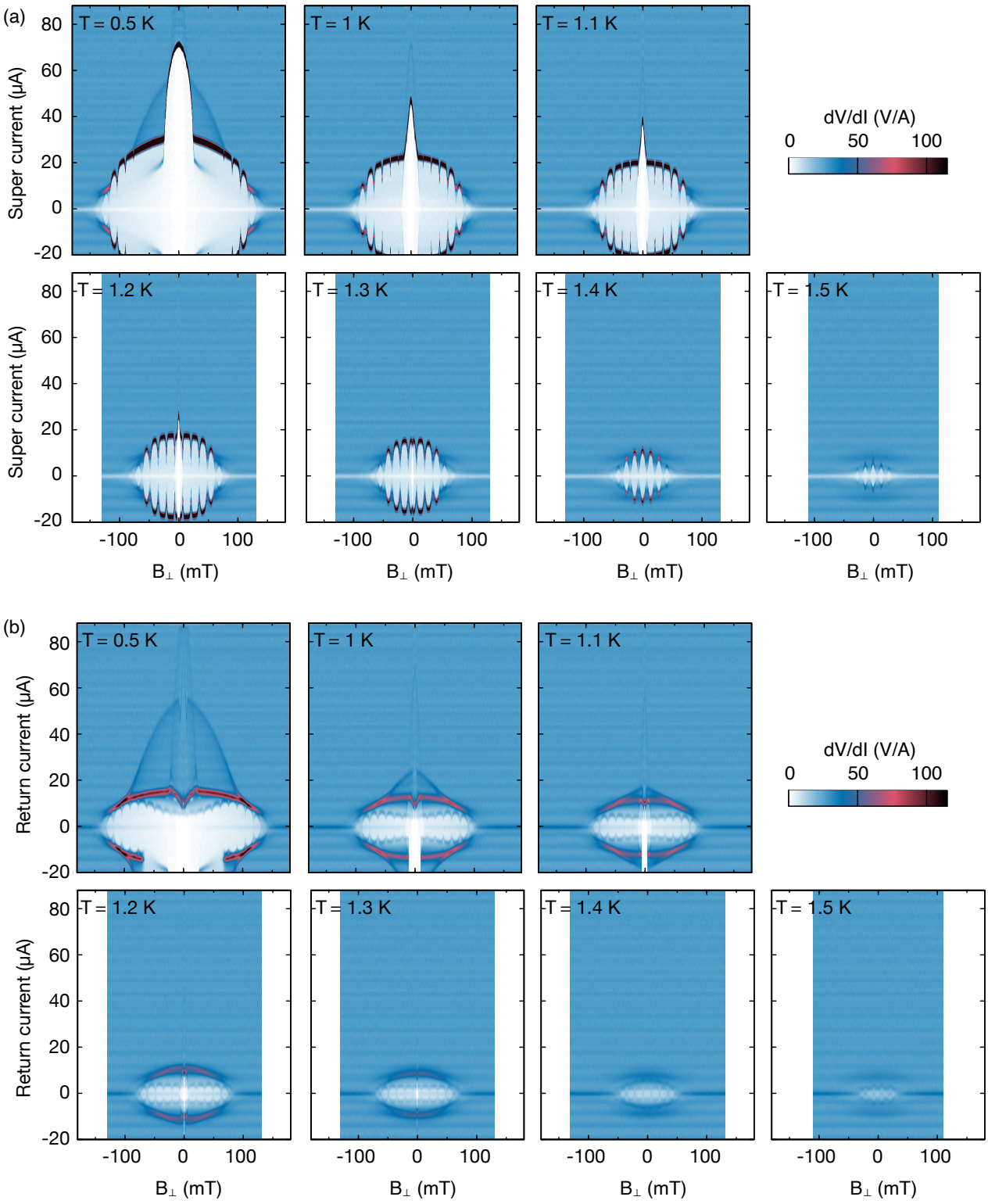

FIG. S3. dV/dI versus $B_\perp$ for the 200 nm radii ring for (a) the super-current and (b) the re-trapping current at temperatures of 0.5-1.5 K. These were determined from the numerical derivative of current voltage traces.

REFERENCES

[1]M. Tinkham, *Introduction to superconductivity* (McGraw-Hill, New York, 1975).

[2]A. Bezryadin, *Superconductivity in Nanowires: Fabrication and Quantum Transport* (John Wiley & Sons, Ltd, Weinheim, Germany, 2012).